Flexural Behaviour of Reinforced Concrete Beams Strengthened with a Composite Reinforcement Layer: BFRP Grid and ECC

Yu-Zhou Zheng[1], Wen-Wei Wang[2], and John C. Brigham[3]

[1] Yu-Zhou Zheng, Ph.D. candidate, Department of Bridge Engineering, School of Transportation, Southeast University, Nanjing, China, Tel:+86 025-83792352, Fax: +86 025-83794100; E-mail: universe2009@126.com

[2] Wen-Wei Wang, Professor (Corresponding author), Department of Bridge Engineering, School of Transportation ,Southeast University, Nanjing, China, Tel:+86 025-83792352, Fax: +86 025-83794100; E-mail: wangwenwei@seu.edu.cn

[3] John C. Brigham, Senior Lecturer, Durham University, School of Engineering and Computing Sciences, Stockton Road, Durham, DH1 3LE, UK, Tel. +44 (0) 191 334 2513, E-mail: john.brigham@durham.ac.uk

Abstract: In this paper, a new strengthening technique for reinforced concrete (RC) beams is proposed by combining Basalt Fibre Reinforced Polymer (BFRP) grid and Engineered Cementitious Composites (ECC) as a composite reinforcement layer (CRL). Five RC beams externally bonded with the CRL at the soffit and one control RC beam were tested to investigate their flexural behaviour. The thickness of BFRP grids (i.e. 1 mm, 3 mm and 5 mm) and the bonded length of CRL (i.e. 400 mm, 450 mm and 500 mm) were selected as two main test parameters in test program, while the width and thickness of CRL were fixed approximately at 200 mm and 30 mm, respectively. The test results showed that there is no clear CRL debonding in the strengthened beams. The two final failure modes were concrete crushing or rupture of the BFRP grids, indicating that the proposed technique is effective in suppressing the debonding of externally bonded materials and fully utilizing the material strengths. An analytical model is also presented to predict the load-deflection responses of the strengthened beams, which was validated through comparisons with the test results.

Keywords: RC beams, Flexural behaviour, Strengthening, Basalt fiber-reinforced polymer (BFRP) grid, ECC.

1. INTRODUCTION

There is tremendous demand for repairing and strengthening of existing concrete structures due to ageing as well as increases in service loads. Externally bonded Fibre Reinforced Polymer (FRP) composites have been gradually introduced as a new construction material for strengthening the concrete structures over the past two decades, and have been shown to have many prominent advantages, such as the high tensile strength, light weight and excellent corrosion resistance of the FRP composites [1-7]. Usually, epoxy resins are used to bond the FRP composites to the surface of concrete structures. However, the bonding behaviour at the FRP-to-concrete interface may deteriorate due to environmental factors, such as moisture, high temperature and fire [8, 9] because of the organic property of the epoxy material. Therefore, some scholars have attempted to utilize inorganic cementitious materials to replace the epoxy resin to develop new fibre composite systems, such as dry fibre sheets bonded with cementitious materials [10-15], fibre-reinforced inorganic polymer (FRIP) composites [16,17] and textile reinforced mortars (TRM) [18-21] for strengthening RC members. The advantages of the inorganic bonding materials are their high resistance to ultraviolet (UV), reduced environmental impact, better resistance to elevated temperature and moisture, as well as better compatibility with the substrate concrete. However, compared to epoxy, inorganic cementitious materials are significantly more brittle and may be difficult to penetrate when fiber sheets/textiles are used as the reinforcing materials [22-29].

In this paper, a new bonded composite system is explored, FRP grid-engineered cementitous composite strengthening system (FRP-ECC strengthening system), in which ECC is applied as a bonding agent between the FRP grid and the concrete substrate. This new system is expected to provide a dual strengthening effect to the original concrete RC beams due to the high strength of the FRP grid reinforcement and the strain-hardening behaviour of the ECC. Meanwhile, the use of ECCs as the bonding adhesive is expected to be able to suppress the intermediate crack-induced debonding failure in typical strengthened beams and avoid local stress concentrations at the interface between the strengthening layer and the substrate concrete due to the multiple crack behaviour of the ECC [30, 31].

2. MATERIAL TENSILE TESTS

2.1 Basalt FRP Grids and ECC

Unidirectional tensile tests were conducted to investigate the mechanical properties for Basalt FRP (BFRP) grids and ECC. The BFRP grid used for enhancing the ECC in this experimental program was produced by Jiangsu Green Materials Vally New Material T&D Co., Ltd, China. Continuous basalt-based untwisted yarns were used as the reinforcing fibres, which were impregnated with epoxy resins to form the longitudinal and transverse BFRP grids. In this grid system, the BFRP reinforcements were arranged at a space of 50 mm center-to-center along the longitudinal and transverse directions, as shown in Fig.1a. Three same coupons in one group with three types of thickness (i.e. 1 mm, 3 mm and 5 mm) were prepared for determining the material behaviour of BFRP gird. The dimensions of each coupon were 1500 mm in length, 200 mm in width and 30 mm in depth.

ECC was made from ordinary Portland cement, fly ash, fine sand, polyvinyl alcohol (PVA) fibre and some additives, and the specifics of the mix are listed in Table 1. The mixed ECC was poured into steel moulds to form three coupons with dimensions of 400 mm (length) ×100 mm (width) ×30 mm (thickness). Displacement-controlled unidirectional tensile tests were then conducted on BFRP grid and ECC coupons. During the tests, the flat BFRP grid and ECC coupons were clamped with two aluminium plates at their two ends to ensure that the coupons were uniformly loaded, as shown in Fig.1b. The loading rate was 0.5 mm/ min.

2.2 Results of Tensile Tests

The tensile stress-strain curves of BFRP grid and ECC are shown in Fig.2a and 2b, respectively, and the failure modes are shown in Fig.2c and 2d, respectively. As expected, the BFRP girds behave in a linear manner up to rupture (Fig.2a). The average tensile strengths of 1 mm, 3 mm and 5 mm thick BFRP grids were 357 MPa, 386 MPa and 416 MPa, respectively, while the average elastic modulus were 51 GPa, 53 GPa and 57 GPa, respectively. As a result, the average elongation were 0.27%, 0.26% and 0.22%, respectively. Unlike BFRP grids, ECC exhibits strain-hardening behavior

associated with the progressive formation of fine cracks until failure (Fig.2b). Furthermore, the gradual propagation of fine cracks in ECC led to a decrease in the tensile stiffness of the ECC coupons. Finally, the ECC coupons failed by rupture or pulling out of the internal PVA fibers at a major crack location. The average tensile strength and rupture strain of the three ECC coupons were 2.75 MPa and 0.99% respectively.

3. FLEXURAL TEST OF RC BEAMS STRENGTHENED WITH CRL

3.1 Details of Beam Specimens

A total of six simply supported reinforced concrete (RC) beams with dimensions of 300 mm in depth, 200 mm in width and 1700 mm in span length were manufactured and subjected to four-point bending tests as shown in Fig.3. The investigated variables included the thickness of BFRP grids and the bond length of composite reinforcement layer (CRL). Table 2 summarizes the details of all test beams. Among the six beams, one was a non-strengthened control beam (CL) and the remaining five were strengthened with a 30 mm thick CRL. Three thicknesses of BFRP grids were applied to reinforce the ECC over-layer: 1 mm thickness for beam BB-1-500, 3 mm thickness for beams BB-3-500, BB-3-450 and BB-3-400, and 5 mm thickness for beam BB-5-500, respectively. In addition, varying lengths of CRL were applied to investigate the effect of bonding length on the final debonding failure of CRL: 500 mm length for beam BB-1-500, BB-3-500 and BB-5-500, 450 mm length for beam BB-3-450 and 400 mm for beam BB-3-400, respectively, as shown in Table 2. The bonding length L_f is defined as the longitudinal distance between the end edge of CRL and nearby loading point as shown in Fig.3.

Four ribbed steel bars of 12 mm in diameter were longitudinally placed into the bottom and top portions of the test beams as the tensile and compressive steel reinforcement, respectively. The thickness of concrete cover was 30 mm for both the top and bottom steel reinforcement. The stirrups were plain round bars of 10 mm diameter and spaced 100 mm center-to-center to avoid shear failure prior to flexural failure.

4

The design strength grade of concrete for the RC beams was C30 according to the Chinese design specification of concrete structures [32]. Ordinary Portland cement, fine and coarse aggregates with the maximum diameter of 20 mm and water were mixed together to form the concrete. The water-cement and sand ratio of concrete were 0.6 and 38%, respectively. During the stage of casting test beams, three cubic samples with dimensions of 150 mm×150 mm×150 mm were reserved to measure the compressive strength of concrete. The average value of 28-day compressive strength for the concrete was 35 MPa.

After the RC beams were cured 28 days and polished with grinding wheels, BFRP grids were firstly fixed on the bottom surface of RC beams through embedded steel bolts. Afterwards, a 30 mm thick ECC layer was casted along the longitudinal direction of the beams to form the CRL. During the process of casting the CRL, three cubic samples with dimension of 70.7 mm×70.7 mm× 70.7 mm were retained to determine the compressive strength of ECC. The average value of 28-day cube compressive strength for the ECC was 31 MPa. The strength for the two grades of steel reinforcement was determined by averaging the measured values of three samples. The mean values of the yielding and ultimate strengths of longitudinal tensile reinforcement (HRB335 grade) were 560 MPa and 684 MPa, respectively, and 471 MPa and 531 MPa for longitudinal compressive reinforcement (HPB235 grade), respectively.

The two-point symmetric loadings separated by 500 mm were applied on the top surface of the beam specimens using a rigid distribution steel girder. The variation of vertical loading was monitored by a load cell connected with a 500-kN hydraulic jack during the whole process of the tests. Five LVDTs were placed at two supports, two loading-points and mid-span section to measure their vertical displacements. Concrete and ECC strains were also measured at the mid-span section using 50-mm-long electrical resistance strain gauges (e.g. gauges No.SG1 to No.SG5 were used for measuring the concrete strains and gauge No.SG6 was applied for detecting the ECC strain) as shown in Fig.4a. One electrical resistance strain gauge (No.SG7) was bonded on the surface of the tensile steel

reinforcement and another (No.SG8) was attached on the BFRP grid to detect their strains at the mid-span section. In order to measure the strain variations of CRL in its end region, nine electric resistance strain gauges with different spacing were attached to the surface of CRL for the strengthened beams BB-3-500, BB-3-450 and BB-3-400, as indicated in Fig. 4b.

3.2 Flexural Test Results

3.2.1 Failure modes and load-displacement responses

The typical flexural failure mode of concrete crushing between two loading points was observed in the control beam CL as shown in Fig.5a. For the strengthened beams BB-1-500, BB-3-500, BB-3-450 and BB-3-400, the rupture of two longitudinal BFRP reinforcements of the grid was observed at the mid-span section and subsequently followed by the concrete crushing in the compressive zone, as shown in Fig.5b. For the strengthened beam BB-5-500 with 5 mm thickness of BFRP grid, it was noted that partial debonding of CRL at the ECC-to-concrete interface was occurred just after the rupture of BFRP grid under one loading point as shown in Fig.5c. The interfacial debonding of CRL propagated about 192 mm from the rupture point of CRL to the mid-span section. Furthermore, many fine cracks uniformly distributed in the CRL regardless of the final failure modes, as shown in Fig.5b and 5c.

For the non-strengthened control beam without CRL (CL), the first crack occurred at the load of 31 kN (approximately 25% of the ultimate load). More flexural and shear cracks were continually formed and propagated obliquely toward the compressive region of the concrete as the load increased. When the load reached 101 kN (approximately 80% of the ultimate load), the longitudinal steel reinforcement yielded, and then the deflection of the mid-span section increased significantly. When the load reached 126 kN, the typical concrete crushing failure occurred, as shown in Fig.5a.

Beam BB-1-500 was strengthened with a 1 mm thick BFRP grid and a 30 mm thick ECC composite layer. The dimensions of the external CRL were 1500 mm in length, 200 mm in width, and 30 mm in thickness. When the load approached 54 kN (approximately 41% of the ultimate load), a relatively

6

small number of flexural cracks formed in the tensile zone of the concrete, and additional fine cracks appeared on the surface of the CRL. With the load increased to 121 kN (approximately 92% of the ultimate load), new concrete flexural cracks formed and the existing concrete cracks propagated mostly vertically toward the top surface of the beam. The mid-span displacement of the strengthened beam significantly increased after the longitudinal steel reinforcement yielded. When the load increased to 131 kN, a slight "crackling" sound from the BFRP grid could be heard and two longitudinal reinforcements of the BFRP grid were ruptured at the mid-span section, but the other two longitudinal reinforcements had not yet failed. After that point, the beam could no longer carry the external load and concrete crushing occurred. It is evident that a multiple cracking phenomenon occurred in the CRL as shown in Fig.5b and 5c.

For all remaining strengthened beams (BB-3-400, BB-3-450, BB-3-500 and BB-5-500), a similar mechanical phenomenon was observed as was described for beam BB-1-500 during the loading process. The load-displacement responses of all tested beams at the mid-span and loading point sections were presented in Figs. 6a and 6b, respectively. A summary of the key quantities at the moments of first cracking, flexural yielding of steel reinforcement, and the ultimate state was listed in Table 3.

Comparing with the control beam CL, the increments of cracking load were from 18 kN for strengthened beam BB-3-400 to 30 kN for strengthened beam BB-3-500, which indicated the effective tensile contribution of the CRL. Furthermore, there was a remarkable increase in the load at the point of yielding and the ultimate state when an external CRL was added. The load increase ranged between 13% to 35% for yielding and 4% to 33% for ultimate compared to the control beam CL. As indicated in Fig.6a and 6b, there was no significant difference in the flexural stiffness of the strengthened beams before the longitudinal steel reinforcement yielded. After yielding, the load-displacement curves showed that the flexural stiffness of the control beam CL was lower than that of the strengthened beams until failure.

3.2.2 Development of strain distribution at the mid-span section

Strain distributions through the depth of control beam (CL) and strengthened beams (i.e. BB-1-500, BB-3-500, BB-5-500, BB-3-450 and BB-3-400) at the mid-span section were showed in Fig.7. As expected, the strain distributions were generally linear before and after concrete cracking. Furthermore, there was no slip between the CRL and the concrete substrate, which indicated satisfactory bonding performance of the interface.

It can be observed from Fig.8 that the load-strain curves of the BFRP grid and the steel reinforcement at the mid-span section for each beam can be divided into three stages. In the first stage, the strains in the BFRP grids were slightly higher than the steel reinforcement strains at the load prior to concrete cracking. In the second stage (after concrete cracking), the increment of strain in the BFRP grid began to exceed those in the steel reinforcement for most of the strengthened beams. In the last stage (the load beyond the yield strength of the steel reinforcement), the strains in both the BFRP grid and the steel reinforcement increased rapidly, however, the strain in the BFRP grid increased more rapidly than that in the steel reinforcement due to the yielding of the ECC and steel reinforcement.

It can be clearly seen from Fig.8 that the strains of steel reinforcement in the strengthened beams were greatly decreased compared to that of non-strengthened beam CL at an equivalent loading level, and it was contributed by the strengthening effect of CRL. It is also indicated that the CRL strengthening system can greatly improve the flexural capacity of RC beams by sharing the tensile stress of internal steel reinforcement.

3.2.3 Analysis of CRL stress at the end region

Debonding failures of FRP strengthened RC beams have been documented by many researchers and can be considered in two categories, i.e. pure flexural debonding of a plate end located in a pure bending region (simply 'flexural debonding') and pure shear debonding of a plate end subjected to a

high shear force but little or no moment (simply 'shear debonding') [33-43]. For a simply–supported CRL strengthened RC beam, the shear debonding can be considered as the control debonding failure if the bond length of CRL is enough (e.g. a CRL end near a support of a simply-supported beam). Therefore, the shear force acted on the CRL plate end is a dominated action and the bending moment can be neglected at the same location [36, 37]. So two analytical models proposed by Smith and Teng [38,39], Teng and Yao[40,41]may be combined to predicate the distribution of shear stress at the CRL-to-concrete interface along the bond length of CRL and the end debonding failure of CRL strengthened RC beams. If the CRL was treated as an externally bonded strengthening reinforcement plate and the ECC layer was regarded as the adhesive layer correspondingly, the shear stress of interface along the longitudinal direction of CRL can be given as follows[38,39]:

$$\tau(x) = m_1 V(x) + \frac{m_2}{\lambda} M(0)e^{-\lambda x} - m_1 P ch(\lambda x)e^{-k} \tag{1}$$

where $V(x)$ is the shear force at the location x defined in Fig.3; $M(0)$ is the bending moment at the location of CRL plate end; P is the applied load acting on the RC beam; $m_1 = \dfrac{G_e y_0}{t_e \lambda^2 E_c I_c}$; $m_2 = \dfrac{G_e y_0}{t_e E_c I_c}$;

$k = \lambda(B-a)$; $\lambda = \sqrt{\dfrac{G_e b_e}{t_e}\left[\dfrac{y_0(y_0+t_e)}{E_c I_c} + \dfrac{1}{E_c I_c}\right]}$; G_e, t_e are the shear modulus and thickness of ECC layer, respectively; y_0 is the distance from the centroid of cross-section to the subsurface of the tested beam; E_c is the elastic modulus of concrete; I_c is the cross sectional moment of inertia of the RC beam; b_e is the width of ECC layer; B and a are the shear-span and the distance from the support to the nearby end edge of CRL plate, respectively, and defined in Fig.3.

In the shear debonding strength model, the maximum debonding shear force was deduced by Teng and Yao as follows [40, 41]:

$$V_{db,s} = V_c + V_e + \varepsilon_{v,e}\overline{V_s} \tag{2}$$

where V_c, V_e and $\varepsilon_{v,e}\overline{V_s}$ are the contributions of concrete, CRL and the internal steel shear reinforcement to the shear capacity of the beam, respectively; V_c can be replaced by the corresponding

expression in ACI specification[44] and $V_c = 0.158 b_c h_0 \sqrt{f_c'} + 17.2 A_s h_0 / a$; b_c and h_0 are the width and

effective depth of section for RC beam, respectively; A_s is the cross-sectional area of the tensile steel

reinforcement; f_c' is the compressive strength of concrete prism ; $\overline{V_s}$ is the shear force carried by the

steel shear reinforcement per unit strain, which is $\overline{V_s} = A_{sv} E_{sv} h_0 / s_v$; A_{sv}, E_{sv} and s_v are the total cross-

sectional area of the steel stirrup, the elastic modulus and the longitudinal spacing of the steel stirrups,

respectively; $\varepsilon_{v,e}$ is effective strain of the steel shear reinforcement and is given as Eq.(3) [40,41]:

$$\varepsilon_{v,e} = \frac{10}{\sqrt{\dfrac{(EI)_{ce} - (EI)_c}{(EI)_c} \dfrac{E_e b_c}{E_c b_e} (\dfrac{t_e}{h_0})^{1.3}}} \tag{3}$$

where $(EI)_{ce}$ and $(EI)_c$ are the flexural rigidities of the cracked section with and without a CRL,

respectively.

It should be noted that the contributions of CRL V_e, expressed in Eq. (2), to the shear capacity of the

beam can be ignored due to its relatively thin thickness to the whole depth of the RC beam.

Substituting Eq. (2) into Eq. (1), the following equation can be used to analyze the distribution of

critical shear stress under the maximum debonding shear force (i.e. debonding shear force):

$$\tau(x) = m_1 V_{db,s} + \frac{m_2}{\lambda} M(0) e^{-\lambda x} - m_1 P ch(\lambda x) e^{-k} \tag{4}$$

Before evaluating the bond behavior at the CRL end region, the distribution of interfacial shear stress

along the bonding length of CRL should be firstly determined on the basis of the measured CRL

strains near the end region. Based on internal force equilibrium in the differential element as shown in

Fig.4c, the mean interfacial shear stress $\tau_{i+1,i}$ between adjacent strain gauges was obtained as [10, 43]:

$$\tau_{i+1,i} = \frac{t_e E_e (\varepsilon_{i+1} - \varepsilon_i)}{\Delta x_{i+1,i}} \quad i \in (1,2,3.....,9) \tag{5}$$

where E_e is the elastic modulus of ECC; ε_i and ε_{i+1} are the measured strains in the ECC layer at

adjacent strain gauge locations i and $i + 1$ which are separated by a distance $\Delta x_{i+1,i}$, as shown in Fig.4c.

The distributions of the critical shear stress for three strengthened beams BB-3-500, BB-3-450 and BB-3-400 can be calculated by Eq.(4). Meanwhile the local shear stress distributions of the CRL-to-concrete interface under three important load levels (i.e. cracking, yielding and ultimate loads) for those three beams can be obtained by Eq.(5). It can be found from Fig.9 that the maximum values of the critical shear stress at the CRL plate end for the test beams BB-3-500, BB-3-450 and BB-3-400 are 3.93 MPa, 4.96 MPa and 6.02 MPa respectively, while the corresponding maximum local shear stress at the same location are only 0.95 MPa for beam BB-3-500, 1.31 MPa for beam BB-3-450 and 1.90 MPa for beam BB-3-400, respectively, which are all far below the critical shear stress at the CRL plate end. Same compared results can be found in any other locations, as shown in Fig.9. The analytical results further indicate that the shear debonding failure is not happen for all CRL strengthened beams and the additional mechanical anchorage or U-shaped jack applied in the FRP strengthening technique for avoiding the plate end debonding is no need in this FRP-ECC strengthening technique.

4 Analytical model

In order to predict the flexural capacity of RC beams strengthened with CRL of BFRP grid and ECC, a theoretical model using the sectional analysis method is presented in this section. The following assumptions are used for the analysis: 1) plane cross-sections remain plane for strengthened beams after loading, 2) the compressive and tensile constitutive model for the concrete and the stress-strain relationship for the steel reinforcement are known as shown in Fig.10a and 10b, respectively, and 3) the tensile strength of concrete will be ignored after cracking.

As seen from the above tensile test results, sufficient performance can be observed only along the main direction of the fibers because BFRP grid is a kind of anisotropic material. Therefore, a linear elastic model is used for the BFRP grid, such that the stress of BFRP grid σ_f is equal to the elastic modulus of BFRP grid E_f multiplied by its strain ε_f (i.e. $\sigma_f = E_f \varepsilon_f$) as shown in Fig.10c.

11

The bilinear strain-hardening model is applied for the ECC, and it can be divided into two stages: the ascend stage and the level stage, as shown in Fig.10d. Simply put, the strain point just before ECC cracking is defined as the cracking strain $\varepsilon_{e,cr}$ and the corresponding stress is defined as the cracking stress f_e, as shown in Fig.10d. When the ECC strain reaches to the ultimate tensile strain ε_{eu}, the tensile coupon is considered to fail. Therefore, the relationship of stress and strain of the ECC can be written as:

$$\begin{cases} \sigma_e = E_e \varepsilon_e & (0 < \varepsilon_e \leq \varepsilon_{e,cr}) \\ \sigma_e = f_e & (\varepsilon_{e,cr} \leq \varepsilon_e \leq \varepsilon_{eu}) \end{cases} \tag{6}$$

where $\varepsilon_{e,cr}$ and ε_{eu} are the cracking strain and ultimate strain of ECC, respectively; f_e is the cracking stress of ECC; E_e is the elastic modulus of ECC; and σ_e is the stress of ECC when the strain is ε_e.

As shown in Fig.11, a RC beam strengthened with CRL can be considered as a composite beam consisting of two sub-elements: the CRL and the RC beam. The internal axial forces can be divided into four parts, C_c and C_t, acting on the centroid of the concrete compressive and tensile zone, respectively; T_s and T_{ef}, contributing as the resultant forces of the steel reinforcement and CRL, respectively, and taken as $T_{ef} = T_f + T_e$, where T_f and T_e are the resultant forces of the BFRP grid and the ECC, respectively.

Applying equilibrium conditions of the compressive and tensile forces acting on the cross-section, the following equation is obtained:

$$C_t + T_s + T_f + T_e - C_c = 0 \tag{7}$$

in which,

$$\begin{cases} C_c = \int_0^{x_a} \sigma_c(\varepsilon_c) b \, dy \\ C_t = \int_0^{h_c - x_a} \sigma_t(\varepsilon_t) b \, dy \\ T_s = \sigma_s A_s \\ T_f = \sigma_f A_f \\ T_e = \sigma_e A_e \end{cases} \tag{8}$$

12

where $\sigma_c(\varepsilon_c)$ is the compressive stress of concrete when the strain is ε_c; $\sigma_t(\varepsilon_t)$ is the tensile stress of concrete when the strain is ε_t; x_a is the depth of the concrete compressive zone; h_c and b are the depth and width of the RC beam, respectively; A_s, A_f and A_e are the cross sectional area of the steel reinforcement, the BFRP grid and the ECC, respectively.

To calculate the tensile stresses of the concrete, the steel reinforcement, the BFRP grid and the ECC, the determined strain of each material element should be firstly obtained. From the strain-geometry relationships as shown in Fig.11, the strain of each material element can be obtained as:

$$
\begin{cases}
\varepsilon_t = \dfrac{h_c - x_a}{x_a}\varepsilon_c \\[2mm]
\varepsilon_s = \dfrac{h_0 - x_a}{x_a}\varepsilon_c \\[2mm]
\varepsilon_f = \varepsilon_e = \dfrac{h_f - x_a}{x_a}\varepsilon_c
\end{cases}
\tag{9}
$$

where ε_t, ε_s, ε_f, ε_e are the tensile strain of the concrete, the steel reinforcement, the BFRP grid and the ECC, respectively; h_f is the distance from the centroid of the BFRP grid to the top face of the strengthened beam.

Substituting Eqs. (8) and (9) into Eq.(7), the following expression of two variables x_a and ε_c are obtained:

$$
\int_0^{h-x_a} \sigma_t(\varepsilon_c)b\,dy + \sigma_s(\varepsilon_c)A_s + \sigma_f(\varepsilon_c)A_f + \sigma_e(\varepsilon_c)A_e - \int_0^{x_a} \sigma_c(\varepsilon_c)b\,dy = 0
\tag{10}
$$

The location of the neutral axis x_a can be obtained by solving Eq. (10) after the concrete compressive strain ε_c is reduced. Taking the moment about the centroid of the concrete compressive zone, the following is obtained:

$$
M = C_t(h_t - y_c) + T_s(h_0 - y_c) + T_f(h_f - y_c) + T_e(h_f - y_c)
\tag{11}
$$

where y_c is the distance from the location of the concrete compressive force to the edge of the compressive concrete zone and can be calculated as:

13

$$y_c = \begin{cases} \dfrac{4\varepsilon_0 - \varepsilon_c}{4(3\varepsilon_0 - \varepsilon_c)} x_a & (0 \le \varepsilon_c \le \varepsilon_0) \\[4mm] \left[1 - \dfrac{\dfrac{1}{2} - \dfrac{1}{12}(\dfrac{\varepsilon_0}{\varepsilon_c})^2}{1 - \dfrac{\varepsilon_0}{3\varepsilon_c}} \right] x_a & (\varepsilon_0 \le \varepsilon_c \le \varepsilon_{cu}) \end{cases} \tag{12}$$

where ε_0 is the strain corresponding to the peak compressive stress of the concrete; ε_{cu} is the ultimate compressive strain of the concrete.

It is difficult to directly solve Eq. (11) if the compressive and tensile forces of each material element are not determined. The following sub-sections will provide the solution details of those forces according to three different states: cracking, yielding and ultimate states of the strengthened beams.

4.1 Cracking state

When the maximum tensile strain of concrete reached to its ultimate strain ε_{tu}, the concrete at the tensile zone will be cracked. It is noted that the ultimate tensile strain ε_{tu} of concrete is assumed to be 0.00015 according to the CEB-FIP specification [45]. Meanwhile, the maximum stress at the edge of the concrete compressive zone is less than $0.3f_c$. Therefore, the concrete can be considered as a linear-elastic material in the compressive zone, and the triangular distributed stress model can be used for calculating the concrete compressive force, as shown in Fig.11a. At this time, the compressive and tensile forces in Eq. (8) can be rewritten as:

$$\begin{cases} C_c = \dfrac{1}{2} E_c \varepsilon_c b x_a \\ C_t = f_t b(h - x_a)(0.95 - 0.5\varepsilon_{t0} / \varepsilon_{tu}) \\ T_s = E_s \varepsilon_s A_s \\ T_f = E_f \varepsilon_f A_f \\ T_e = E_e \varepsilon_e A_e \end{cases} \tag{13}$$

where E_c and E_s are the elastic modulus of the concrete and the steel reinforcement, respectively; f_t is the tensile strength of the concrete; ε_{t0} is the strain of the tensile concrete corresponding to the stress $0.9f_t$.

Substituting Eqs. (9) and (13) into Eq.(7), the following formula can be obtained:

$$A_1 x_a^2 + B_1 x_a + C_1 = 0 \tag{14}$$

in which,

$$\begin{cases} A_1 = 0.5 E_c b \varepsilon_{tu} - 0.69 f_t b \\ B_1 = 1.37 f_t bh + \varepsilon_{tu} (E_s A_s + E_f A_f + E_e A_e) \\ C_1 = -0.69 f_t bh^2 - \varepsilon_{tu} (E_s A_s h_0 + E_f A_f h_f + E_e A_e h_f) \end{cases} \tag{15}$$

The location of neutral axis x_a can be deduced by solving Eq. (14), then substituting x_a into Eq. (12), the distance y_c from the location of concrete compressive force to the edge of compressive zone was obtained and the cracking moment of strengthened beam can be given as:

$$M_{cr} = C_t (h_t - \frac{1}{3} x_a) + T_s (h_0 - \frac{1}{3} x_a) + T_f (h_f - \frac{1}{3} x_a) + T_e (h_f - \frac{1}{3} x_a) \tag{16}$$

4.2 Yielding state

According to the fundamental assumptions, the tensile force of the concrete is neglected after cracked. Thus, the total tensile forces of the cross section are shared by the steel reinforcement, the BFRP grid and the ECC, as shown in Fig.11b. At this state, the tensile stress of the steel reinforcement is equal to its yielding load f_y. Moreover, the tensile stress of the ECC is considered to be equal to its cracking stress f_e as a result of large strain achieved in the ECC layer. Consequently, the force of each material in Eq. (8) can be rewritten as:

$$\begin{cases} C_c = \int_0^{x_a} \sigma_c (\varepsilon_c) b dy \\ T_s = f_y A_s \\ T_f = E_f \varepsilon_f A_f \\ T_e = f_e A_e \end{cases} \tag{17}$$

The compressive force of the concrete can be obtained by integrating the concrete nonlinear stress-strain model (Fig.10a). And the following formulas can be deduced:

$$\begin{cases} A_2 x_a^3 + B_2 x_a^2 + C_2 x_a + D_2 = 0 & (0 \le \varepsilon_c \le \varepsilon_0) \\ A_2' x_a^2 + B_2' x_a + C_2' = 0 & (\varepsilon_0 \le \varepsilon_c \le \varepsilon_{cu}) \end{cases} \tag{18}$$

in which,

$$\begin{cases} A_2 = 3f_c b\varepsilon_0 \varepsilon_{sy} + f_c b\varepsilon_{sy}^2 \\ B_2 = 3\varepsilon_0^2(f_y A_s + E_f A_f \varepsilon_{sy} + f_e A_e) - 3f_c bh_0 \varepsilon_0 \varepsilon_{sy} \\ C_2 = -3E_f \varepsilon_0^2 \varepsilon_{sy} A_f (h_f + h_0) - 6\varepsilon_0^2 h_0 (f_y A_s + f_e A_e) \\ D_2 = 3E_f \varepsilon_0^2 \varepsilon_{sy} A_f h_f h_0 + 3\varepsilon_0^2 h_0^2 (f_y A_s + f_e A_e) \\ A_2' = -3f_c b\varepsilon_{sy} - 3f_c b\varepsilon_0 \\ B_2' = 3f_c bh_0 \varepsilon_{sy} + 6f_c bh_0 \varepsilon_0 + 3E_f A_f \varepsilon_{sy} + 3\varepsilon_{sy} f_y A_s + 3\varepsilon_{sy} f_e A_e \\ C_2' = -3f_c bh_0^2 \varepsilon_0 - 3E_f \varepsilon_{sy} A_f h_f - 3\varepsilon_{sy} h_0 (f_y A_s + f_e A_e) \end{cases} \tag{19}$$

The depth of neutral axis x_a can be obtained by solving Eq. (18) after replace the corresponding coefficients in Eq. (19). Then substituting x_a into Eq. (12), the distance y_c from the location of concrete compressive force to the edge of compressive zone can be obtained and then the yielding moment of strengthened beam can be given as:

$$M_y = T_s\left(h_0 - y_c\right) + T_f\left(h_f - y_c\right) + T_e\left(h_f - y_c\right) \tag{20}$$

4.3 Ultimate state

As discussed for the test results, the failure modes of the strengthened beams were concrete crushing or rupture of the BFRP grid according to the different amounts of the BFRP grid reinforcement. Therefore, two cases, concrete crushing and BFRP grid rupture, are considered in the analytical model.

4.3.1 Case 1-concrete crushing

The ultimate strength of the concrete compressive zone is achieved prior to rupture of the BFRP grid after yielding of the longitudinal steel reinforcement, such that $\varepsilon_c = \varepsilon_{cu} = 0.0033$, $\varepsilon_s > \varepsilon_{sy} = f_y / E_s$ and $\varepsilon_f \leq \varepsilon_{fu}$, as shown in Fig.11c. Therefore, the equivalent rectangular stress block can be used for calculating the compressive force of the concrete and the tensile forces of the steel reinforcement, the BFRP grid and the ECC can be given as:

$$\begin{cases} C_c = \alpha\beta f_c bx_a \\ T_f = E_f \varepsilon_f A_f \\ T_s = f_y A_s + E_2\left(\varepsilon_s - \varepsilon_{sy}\right)A_s \\ T_e = f_e A_e \end{cases} \tag{21}$$

where E_2 is the slope of steel reinforcement stress-strain curve after yielding and taken as $E_2=0.01E_s$; ε_{sy} is the yield strain of the steel reinforcement; α and β are the coefficients of concrete equivalent stress block and taken as $\alpha = 1.0$, $\beta = 0.8$ [32,44].

Substituting Eqs. (9) and Eq.(21) into Eq.(7), the following formulas can be deduced:

$$A_3 x_a^2 + B_3 x_a + C_3 = 0 \tag{22}$$

in which,

$$\begin{cases} A_3 = 0.8 f_c b \\ B_3 = E_2 \varepsilon_{sy} A_s + E_2 A_s \varepsilon_{cu} - f_y A_s - f_e A_e + E_f \varepsilon_{cu} A_f \\ C_3 = -E_f \varepsilon_{cu} A_f h_f - E_2 \varepsilon_{cu} A_s h_0 \end{cases} \tag{23}$$

The depth of neutral axis x_a can be obtained by solving Eq. (22), then substituting x_a into Eq. (12), the distance y_c from the location of concrete compressive force to the edge of compressive zone can be obtained and the ultimate moment of strengthened beam can be rewritten as:

$$M_u = T_s(h_0 - y_c) + T_f(h_f - y_c) + T_e(h_f - y_c) \tag{24}$$

4.3.2 Case2-rupture of BFRP grid

After yielding of the longitudinal tensile steel reinforcement, the ultimate strength of the BFRP grid is firstly reached before concrete crushing, i.e. $\varepsilon_c < \varepsilon_{cu}$ and $\varepsilon_f = \varepsilon_{fu}$. In this case, the equivalent rectangular stress block of concrete is not suitable for calculating the compressive force. Subsequently, the force of each material in Eq. (8) can be written as:

$$\begin{cases} C_c = \int_0^{x_a} \sigma_c(\varepsilon_c) b \, dy \\ T_s = f_y A_s + E_2(\varepsilon_s - \varepsilon_{sy}) A_s \\ T_f = f_{fu} A_f \\ T_e = f_e A_e \end{cases} \tag{25}$$

Substituting Eqs. (9) and (25) into Eq.(7) produces:

$$\begin{cases} A_4 x_a^3 + B_4 x_a^2 + C_4 x_a + D_4 = 0 & (0 \le \varepsilon_c \le \varepsilon_0) \\ A_4' x_a^2 + B_4' x_a + C_4' = 0 & (\varepsilon_0 \le \varepsilon_c \le \varepsilon_{cu}) \end{cases} \tag{26}$$

in which,

$$\begin{cases} A_4 = f_c b \varepsilon_{fu}^2 + 3 f_c b \varepsilon_0 \varepsilon_{fu} \\ B_4 = -3 f_c b h_f \varepsilon_0 \varepsilon_{fu} + 3 \varepsilon_0^2 (f_y A_s - E_2 \varepsilon_{sy} A_s + E_2 \varepsilon_{fu} A_s + f_{fu} A_f + f_e A_e) \\ C_4 = -6 \varepsilon_0^2 h_f (f_y A_s - E_2 \varepsilon_{sy} A_s + f_{fu} A_f + f_e A_e) - 3 E_2 \varepsilon_0^2 \varepsilon_{fu} A_s h_0 - 3 E_2 \varepsilon_0^2 \varepsilon_{fu} A_s h_f \\ D_4 = -3 E_f \varepsilon_0^2 \varepsilon_{sy} A_f h_f h_0 - 3 \varepsilon_0^2 h_0^2 (f_y A_s + f_e A_e) \\ A_4{}' = 3 f_c b \varepsilon_{fu} + f_c b \varepsilon_0 \\ B_4{}' = -[3 f_c b \varepsilon_{fu} h_f + 2 f_c b \varepsilon_0 h_f + 3 \varepsilon_{fu} (f_y A_s - E_2 \varepsilon_{sy} A_s + f_{fu} A_f + f_e A_e) + 3 E_2 \varepsilon_{fu}^2 A_s] \\ C_4{}' = f_c b \varepsilon_0 h_f^2 + 3 \varepsilon_{fu} h_f (f_y A_s - E_2 \varepsilon_{sy} A_s + f_{fu} A_f + f_e A_e) + 3 E_2 \varepsilon_{fu}^2 A_s h_f \end{cases} \tag{27}$$

The depth of neutral axis x_a can be obtained by solving Eq. (26) after replacing the corresponding coefficients in Eq. (27), then substituting x_a into Eq. (12), the distance y_c from the location of concrete compressive force to the edge of compressive zone can be obtained and the yielding moment of strengthened beam can be given as:

$$M_u = T_s (h_0 - y_c) + T_f (h_f - y_c) + T_e A_e (h_f - y_c) \tag{28}$$

4.4 Displacement of strengthened beam

For a strengthened beam, the deflection can be obtained using traditional mechanics principles provided that the sectional flexural stiffness is known. However, it is difficult to accurately determine the flexural stiffness of a strengthened beam after the concrete and ECC have cracked. It is well known that the sectional stiffness will decrease and unequally distributed along the whole longitudinal direction of strengthened beam. For simplicity, the equivalent flexural stiffness of strengthened beam B_{eq} in the pure bending region can be applied into the calculation of deflection and it is equal to the external flexural moment of strengthened beam M_x divided by the mean sectional curvature φ_m corresponding to the flexural moment M_x (i.e. $B_{eq} = M_x / \varphi_m$) [46-48].

Assuming the relationship of mean sectional curvature φ_m and external moment M_x is tri-linear throughout the different states, as shown in Fig.12, the mean sectional curvature φ_m can be given as [47,49-51]:

$$\varphi_m = \begin{cases} \dfrac{M_x}{M_{cr}}\varphi_{cr} & (0 < M_x \le M_{cr}) \\[2ex] \dfrac{M_x - M_{cr}}{M_y - M_{cr}}\varphi_y & (M_{cr} < M_x \le M_y) \\[2ex] \varphi_y + \dfrac{M_x - M_y}{M_u - M_y}(\varphi_u - \varphi_y) & (M_y < M_x \le M_u) \end{cases} \qquad (29)$$

where φ_{cr}, φ_y and φ_u are the mean sectional curvature of the strengthened beam at cracking, yielding

and ultimate state, respectively, and given as:

$$\begin{cases} \varphi_{cr} = \dfrac{\varepsilon_{c.cr} + \varepsilon_{s.cr}}{h_0} \\[2ex] \varphi_y = \dfrac{\varepsilon_{c.y} + \varepsilon_{s.y}}{h_0} \\[2ex] \varphi_u = \dfrac{\varepsilon_{c.u} + \varepsilon_{s.u}}{h_0} \end{cases} \qquad (30)$$

where $\varepsilon_{c.cr}, \varepsilon_{c.y}$ and $\varepsilon_{c.u}$ are the concrete compressive strain at the extreme compression edge for the

cracking, yielding and ultimate state, respectively; $\varepsilon_{s.cr}, \varepsilon_{s.y}$ and $\varepsilon_{s.u}$ are the strain of the longitudinal

tensile steel reinforcement at the cracking ,yielding and ultimate state, respectively.

Having determined the mean sectional curvature, the equivalent flexural stiffness can be obtained

when the strengthened beams are in the different states. Then the displacement of the strengthened

beams can be deduced by using the traditional structural mechanics theory. To ensure accurate

calculations, a computer program was developed to perform the numerical analysis. The outputs from

the program were used to calculate the loads and displacements of all test beams at different states

during the whole test process. The comparison of characteristic values, including the predicted loads

and the displacements at the mid-span section for three states are listed in Tables 3 and Table 4, and

the load-displacement curves for the mid-span and loading point sections are also shown in Fig.6a and

Fig.6b. In addition, a comparison between the measured strains of the steel reinforcement and the

BFRP grid of all test beams at mid-span section and those calculated using the predictive model are

presented in Fig.8. It is noted that all characteristic values in the constitutive relationships for the

concrete, steel reinforcement, BFRP grid and ECC are selected from the corresponding material tests shown in Fig.10.

It can be seen from Table 3 and Table 4 that the loads and mid-span section displacements at different states are well predicted. The average ratios of the predicted crack, yielding and ultimate loads (i.e. $P_{cr,e}, P_{y,e}$ and $P_{u,e}$) to the corresponding experimental ones (i.e. $P_{cr,p}$, $P_{y,p}$ and $P_{u,p}$) are 0.99, 1.05 and 0.96, respectively, and the COVs are 0.13, 0.03 and 0.04, respectively. As for the corresponding displacements, the average ratios of the predicted values (i.e. $D_{cr,e}, D_{y,e}$ and $D_{u,e}$) to the corresponding experimental ones (i.e. $D_{cr,p}$, $D_{y,p}$ and $D_{u,p}$) are 0.84, 0.98 and 0.86, respectively, and the COVs are 0.25, 0.06 and 0.19, respectively. Moreover, the calculated strains of all materials are similarly predicted in comparison to the experimental results with an acceptable degree of accuracy, as shown in Fig.8.

5. Conclusions

A new strengthening technique for RC beams is proposed by combining BFRP grid and ECC as a composite externally bonded reinforcement layer. Five such strengthened beams and one control beam were tested to investigate the mechanical behavior of the strengthened beams. The following conclusions can be drawn:

(1) The typical failure mode of concrete crushing was occurred in the control beam CL, while the rupture of BFRP grid was observed in the remaining five strengthened beams. After the RC beam externally strengthened with composite reinforcement layer, the cracking, yielding and ultimate loads were greatly improved compared to that of the control beam.

(2) The multi-point cracking phenomenon of CRL was obviously presented in all strengthened beams after the fine cracks uniformly formed in the CRL. Moreover, there was no slip between the CRL and concrete substrate, which indicates that the proposed FRP-ECC strengthening system is an effective technique to suppress the debonding of externally bonded materials.

(3) The maximum measured stress values of CRL at the end region were far below the calculated values predicted by the model of Teng and Yao et al. Consequently, the end debonding failure of CRL can be effectively avoided in the FRP-ECC strengthening system.

(4) An analytical method was developed for predicting the load capacity and mid-span deflection of RC beam strengthened with CRL and its validity was demonstrated through comparisons with test results.

References

[1] Wang WW, Dai JG, Harries KA, Zhang L. Prediction of prestress losses in RC beams externally strengthened with prestressed CFRP sheets/plates. J REINF PLAST COMP. 2014; 33(8)：699-713.

[2] Wang WW, Dai JG, Harries KA. Performance evaluation of RC beams strengthened with an externally bonded FRP system under simulated vehicle loads. J BRIDGE ENG. 2013; 18(1)：76-82.

[3] Wang WW, Dai JG, Harries KA. Intermediate crack-induced debonding in RC beams externally strengthened with prestressed FRP laminates. J REINF PLAST COMP. 2013; 32(23)：1842-57.

[4] Hashemi S, Al-Mahaidi R. Experimental and finite element analysis of flexural behavior of FRP-strengthened RC beams using cement-based adhesives. CONSTR BUILD MATER. 2012; 26(1)：268-73.

[5] Wang WW, Dai JG, Harries KA, Bao Q. Prestress losses and flexural behavior of reinforced concrete beams strengthened with post-tensioned CFRP sheets. J COMPOS CONSTR. 2012; 16(2)：207-16.

[6] Wang WW, Li G. Experimental study and analysis of RC beams strengthened with CFRP laminates under sustaining load. INT J SOLIDS STRUCT. 2006; 43(6)：1372-87.

[7] Wang WW, Li G. Experimental study of RC beams strengthened with CFRP sheets under sustaining loads. J WUHAN UNIV TECHNOL. 2006; 21(3)：82-5.

[8] Hashemi S, Al-Mahaidi R. Flexural performance of CFRP textile-retrofitted RC beams using cement-based adhesives at high temperature. CONSTR BUILD MATER. 2012; 28(1)：791-7.

[9] Gamage JCPH, Al-Mahaidi R, Wong MB. Bond characteristics of CFRP plated concrete members under elevated temperatures. COMPOS STRUCT. 2006; 75(1-4SI)：199-205.

[10] Zhang L,Wang WW, Harries KA, Tian J.Bonding behavior of wet-bonded GFRP-Concrete interface. J COMPOS CONSTR.2014 ;(04015001):1-14.DOI:10.1061/ (ASCE) CC.1943-5614.0000550.

[11] Hashemi. S, Al-mahaidi R. Cement based bonding material for FRP strengthening of concrete structures. Proceedings of the 9th international symposium on fiber-reinforced polymer reinforcement for concrete structures (FRPRCS-9). 2009, Sydney, Australia.

[12] Toutanji H, Zhao L, Zhang Y. Flexural behavior of reinforced concrete beams externally strengthened with CFRP sheets bonded with an inorganic matrix. ENG STRUCT. 2006; 28(4)：557-66.

[13] Kurtz. S, Palaguru P. Comparison of inorganic and organic matrices for strengthening of RC beams with carbon sheets. J. STRUCT. ENG., 2001; 127(1)：35-72.

[14] Kolsch. H. Carbon fiber cement matrix (CFCM) overlay system for masonry strengthening. J COMPOS CONSTR. 1998; 12(2)：105-9.

[15] Dai JG, Yokota H, Iwanami M, Kato E. Experimental investigation of the influence of moisture on the bond behavior of fiber reinforced polymer (FRP) to concrete interfaces. J COMPOS CONSTR. 2010; 14(6)：834-44.

[16] Dai JG, Munir S, Ding Z. Comparative study of different cement-based inorganic pastes towards the development of FRIP strengthening technology. J COMPOS CONSTR. 2014; 18(3):1-10.

[17] Ding Z, Dai JG, Muner S. Study on an improved phosphate cement binder for the development of fiber-reinforced inorganic polymer composites. POLYMERS-BASEL. 2014; 6(11)：2819-31.

[18] Escrig C, Gil L, Bernat-Maso E, Puigvert F. Experimental and analytical study of reinforced concrete beams shear strengthened with different types of textile-reinforced mortar. CONSTR BUILD MATER. 2015; 83:248-60.

[19] D Ambrisi A, Feo L, Focacci F. Experimental and analytical investigation on bond between Carbon-FRCM materials and masonry. COMPOSITES PART B: ENGINEERING. 2013; 46:15-20.

[20] D Ambrisi A, Francesco F. Flexural strengthening of RC beams with cement-based composites. J COMPOS CONSTR. 2011; 15(5)：707-20.

[21] Xu SL, Yin S. Analytical theory of flexural behavior of concrete beam reinforced with textile-combined steel. SCIENCE CHINA TECHNOLOGICAL SCIENCE. 2010; 53(6)：1700-10.

[22] Maalej M, Leong KS. Engineered cementitious composites for effective FRP-strengthening of RC beams. COMPOS SCI TECHNOL. 2005; 65(7-8)：1120-8.

[23] Wu HC, Sun PJ, Teng JM. Development of fiber reinforced cement based composite sheets for structural retrofit. J. MATER. CIV. ENG., 2010; 22(6), 572–579.

[24] Zheng W, Zhu J. Progress of research on concrete structures strengthened with CFRP sheets bonded with inorganic cementitious materials. JOURNAL OF BUILDING STRUCTURES. 2013; 34(06)：1-12. (In Chinese)

[25] Zhu J, Zheng W. Interfacial shear performance in FRP strengthened concrete structures using AASCM as adhesive. JOURNAL OF SOUTHEAST UNIVERSITY (Natural Science Edition). 2012; 42(05)：962-9. (In Chinese)

[26] Lin W, Sun W, Li Z. Direct shear study of strengthening layer made of continuous carbon fiber fabric-magnesium oxychloride cement paste. JOURNAL OF BUILDING MATERIALS. 2011; 14(01)：106-10. (In Chinese)

[27] Xu, SL, Li QH, Li HD. An experimental study on the flexural properties of carbon textile reinforced. CHINA CIVIL ENGINEERING JOURNAL. 2007; 40(12)：69-76. (In Chinese)

[28] Triantafillou TC, Papanicolaou CG. Shear strengthening of reinforced concrete members with textile reinforced mortar (TRM) jackets. MATER STRUCT. 2006; 39(1)：93-103.

[29] Triantafillou TC, Papanicolaou CG. Textile reinforced mortars (TRM) versus fiber reinforced polymer (FRP) as strengthening materials of concrete structures. Proceedings of the 7th International Symposium on Fiber-Reinforced (FRP) Polymer Reinforcement for concrete Structures (FRPRCS-7): ACI SP-230-6, 2005.

[30] Fischer G, Li VC. Effect of fiber reinforcement on the response of structural members. ENG FRACT MECH. 2007; 74(1-2)：258-72.

[31] Ranade R, Li VC, Heard WF. Tensile rate effects in high strength-high ductility concrete. CEMENT CONCRETE RES. 2015; 68：94-104.

[32] Ministry of Housing and Urban-Rural Development of the People's Republic of China (MOHURD). Code for design of concrete structures. (GB50010-2010).Beijing: China Building Industry Press, 2010. (In Chinese)

[33] Oehlers DJ, Visintin P, Lucas. W. Flexural Strength and Ductility of FRP-Plated RC Beams: Fundamental Mechanics Incorporating Local and Global IC Debonding. J COMPOS CONSTR. 2015; 4015046.

[34] Smith ST, Teng JG. FRP-strengthened RC beams. I: review of debonding strength models. ENG STRUCT. 2002;24(4)：385-95.

[35] Smith ST, Teng JG. FRP-strengthened RC beams. II: assessment of debonding strength models. ENG STRUCT. 2002;24(4)：397-417.

[36] Zhang SS, Teng JG. Finite element analysis of end cover separation in RC beams strengthened in flexure with FRP. ENG STRUCT. 2014; 75:550-60.

[37] Teng JG, Chen JF. Mechanics of debonding in FRP-plated RC beams. PROCEEDINGS OF THE INSTITUTION OF CIVIL ENGINEERS-STRUCTURES AND BUILDINGS. 2009; 162(5):335-45.

[38] Smith ST, Teng JG. Interfacial stresses in plated beams. Engineering Structures.2001; 23:857-71.

[39] Teng JG, Chen JF, Smith ST, Lam L. FRP strengthened RC structures. England: John Wiley and Sons.2002.

[40]Yao J, Teng J G. Plate end debonding in FRP-plated RC beams—I: Experiments. Engineering Structures.2007; 29:2457-71.

[41] Teng J G, Yao J. Plate end debonding in FRP-plated RC beams—II: Strength model. Engineering Structures. 2007; 29(10): 2472-2486.

[42] Dai JG, Ueda T, Sato Y. Development of the nonlinear bond stress-slip model of fiber reinforced plastics sheet-concrete interfaces with a simple method [J]. JOURNAL OF COMPOSITES FOR CONSTRUCTION. 2005; 9(1): 52-62.

[43] Dai JG, Ueda T, Sato Y. Unified Analytical Approaches for Determining Shear Bond Characteristics of FRP-Concrete Interfaces through Pullout Tests [J]. JOURNAL OF ADVANCED CONCRETE TECHNOLOGY. 2006; 4(1): 133-145.

[44] American Concrete Institute (ACI). Building code requirements for structural concrete and commentary (ACI 318M-05). Detroit: American Concrete Institute, 2005.

[45] Comité Euro-International du Béton. CEB-FIP model code 1990. London: Thomas Telford, 1993.

[46] Xu.SL, Yin.SP, Cai.XH. Investigation on flexural behavior of reinforced concrete beam strengthened with textile-reinforced concrete. CHINA CIVIL ENGINEERING JOURNAL. 2011; 44(4):23-34. (In Chinese)

[47] American Concrete Institute (ACI). Guide for the design and construction of externally bonded FRP system for strengthening concrete structures. Detroit: American Concrete Institute, 2000.

[48] Kim J, Kwon M, Seo H, Lim J. Experimental study of torsional strength of RC beams constructed with

HPFRC composite mortar. CONSTR BUILD MATER. 2015; 91:9-16.

[49] Maalej M, Leong KS. Effect of beam size and FRP thickness on interfacial shear stress concentration and failure mode of FRP-strengthened beams. COMPOS SCI TECHNOL. 2005; 65(7–8):1148-58.

[50] Wang WW. Technology and application of FRP reinforced concrete structures. Beijing: China Architecture and Building Press, 2007. (In Chinese)

[51] El-Mihilmy MT, Tedesco. JW. Analysis of reinforced concrete beams strengthened with FRP laminates. J STRUCT ENG. 2000; 126(6)：684-91.
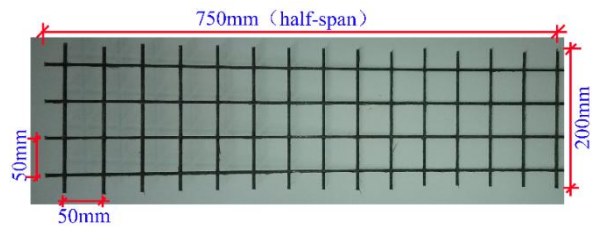
(a) BFRP grid
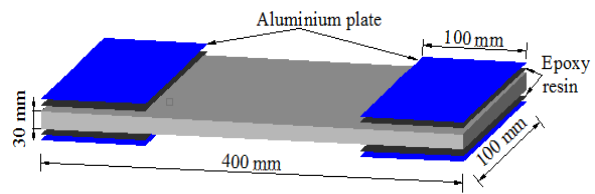
(b) ECC

Fig. 1 Details of BFRP grid and ECC coupons
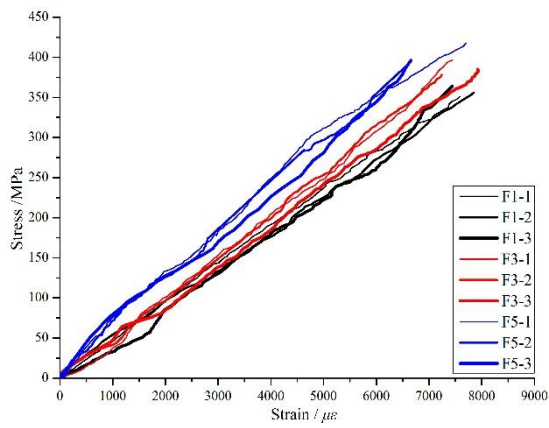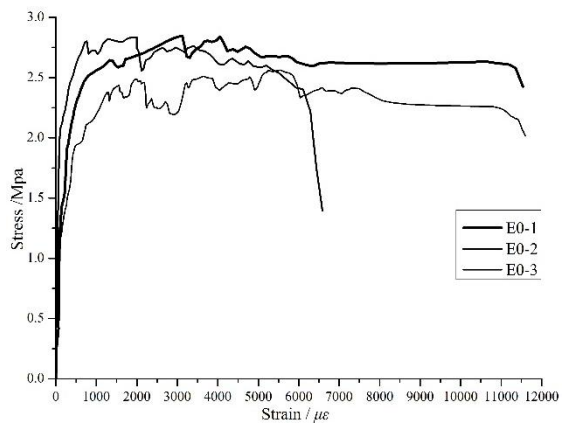
(a) BFRP grid   (b) ECC

(c) Rupture of BFRP grid

(d) Failure of ECC

Fig.2 Tensile coupons and test results
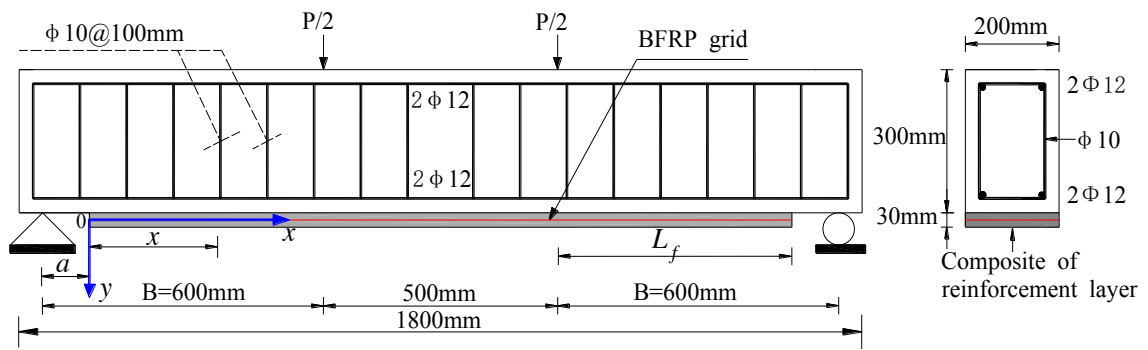
Fig.3 Details of strengthened beams
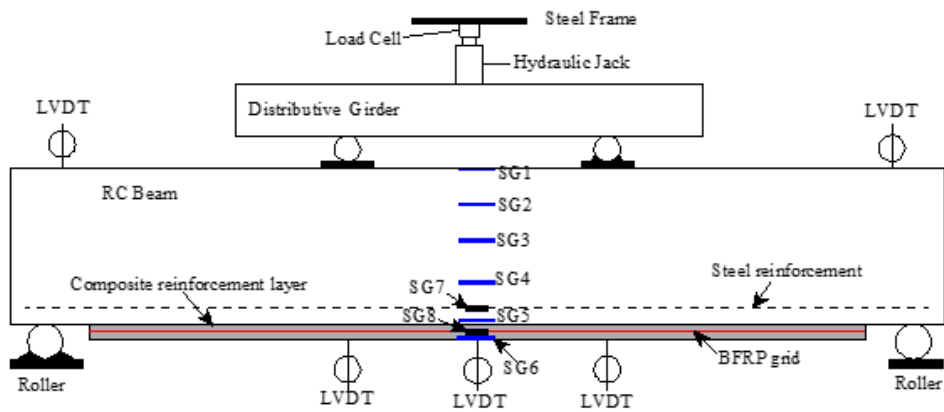
(a) Locations of measuring points for strengthened beam
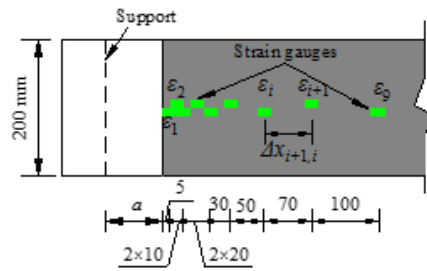
(b) Positions of strain gauges on soffit CRL (unit: mm)
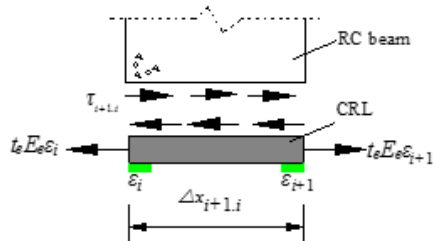
(c) Equilibrium relationship of the isolated body

Fig.4 Details of the test setup
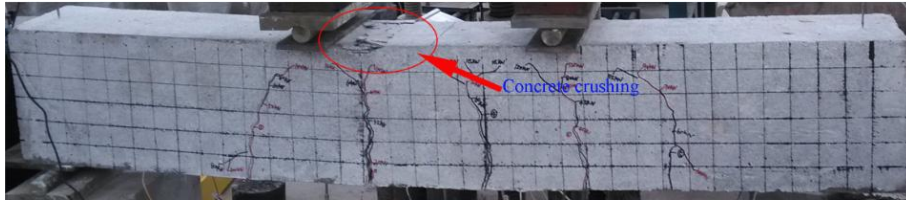
(a) Concrete crushing

(b) Concrete crushing after the rupture of BFRP grid
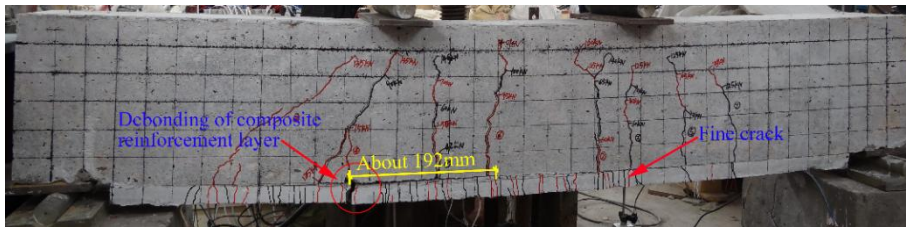
(c) Partial debonding of CRL after the rupture of BFRP grid

Fig.5 Failure modes of test beams
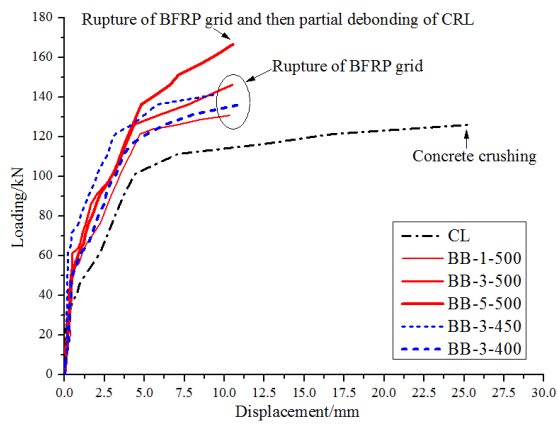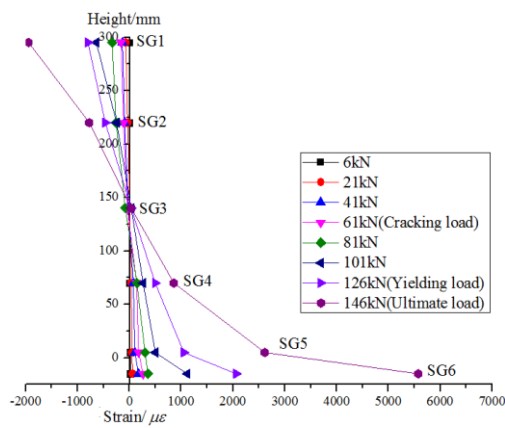
(a) Mid-span section
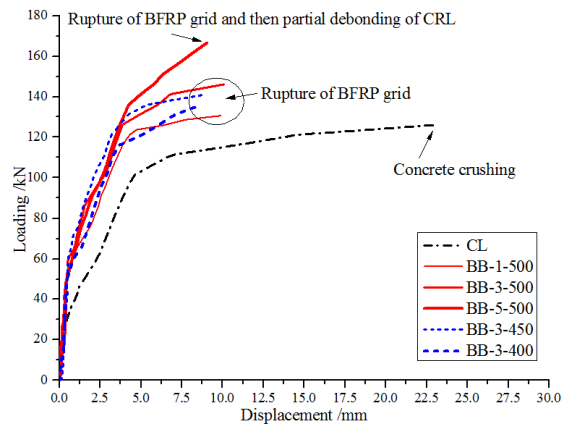
(b) Loading point section

Fig.6 Load-displacement curves of all test beams
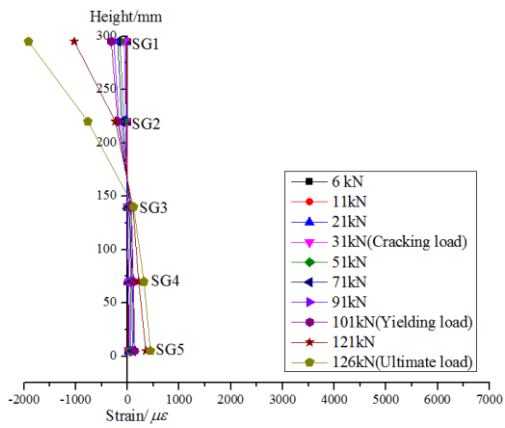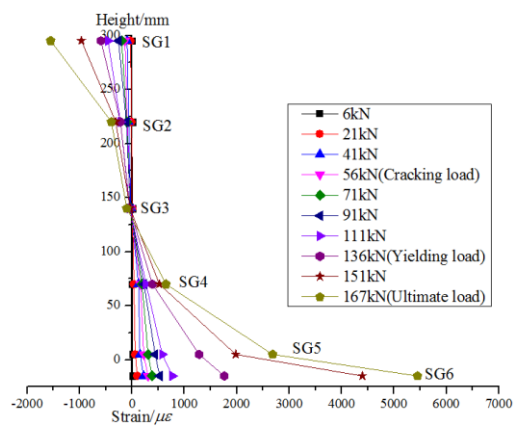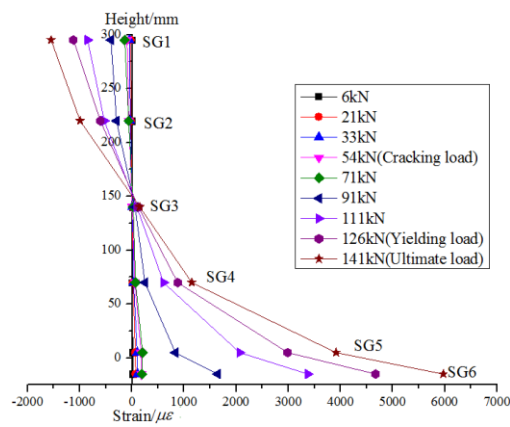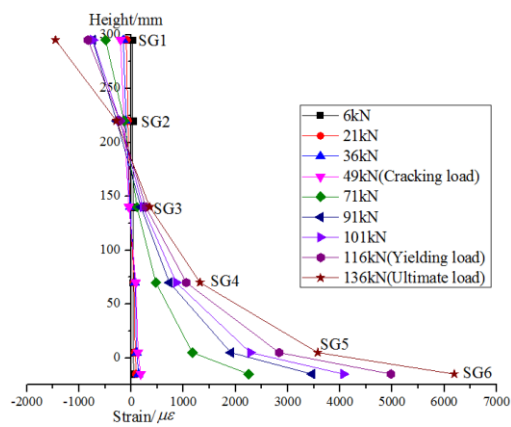
(a) CL
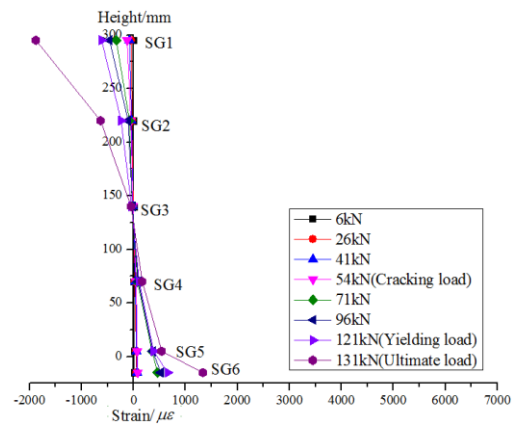
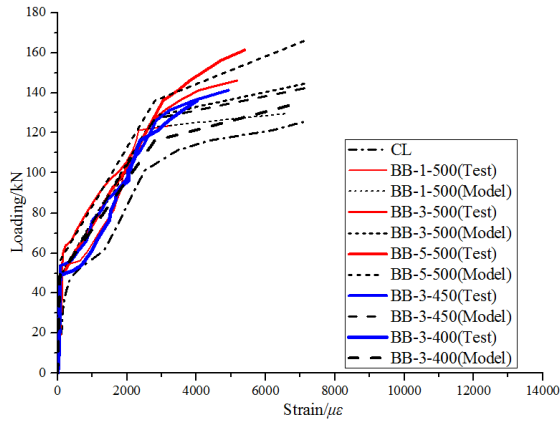(b) BB-1-500

(c) BB-3-500
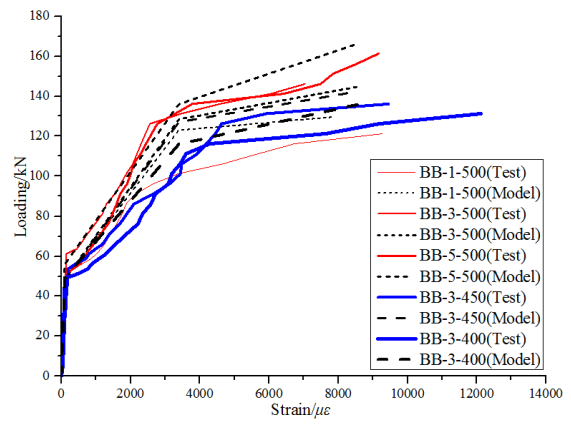
(d) BB-5-500

(e) BB-3-450

(f) BB-3-400

Fig.7 Strain distributions of test beam at the mid-span section
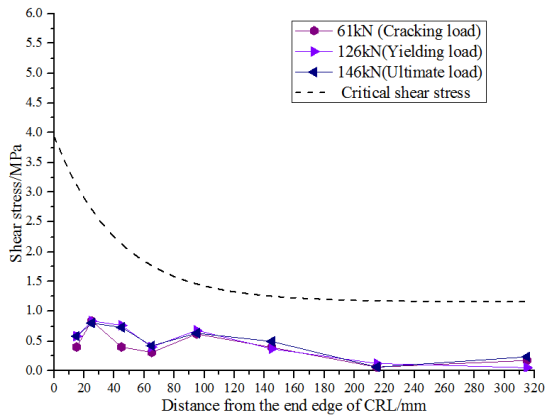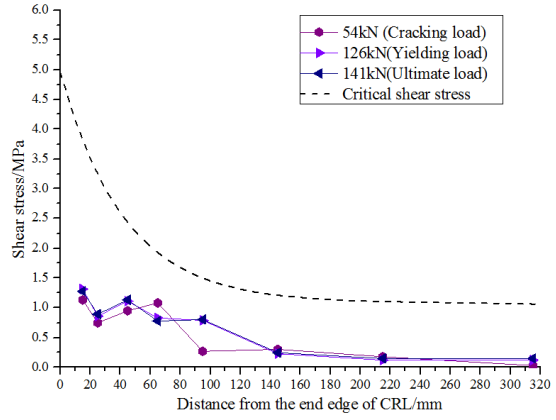
(a) Steel reinforcement   (b) FRP grid

Fig.8 Comparisons of strains in BFRP grid and steel reinforcement at the mid-span section

(a) Beam BB-3-500   (b) Beam BB-3-450
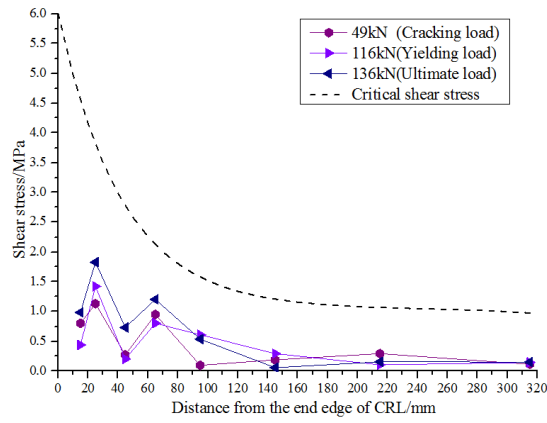
(c)Beam BB-3-400

Fig.9 Shear stress distribution of CRL-to concrete interface at the end region

$$\sigma_c = f_c[2\frac{\varepsilon_c}{\varepsilon_0} - (\frac{\varepsilon_c}{\varepsilon_0})^2]$$

$$\sigma_t = E_c\varepsilon_{tx}$$

$$0.9f_t$$

$$\sigma_t = 0.9f_t + 0.1f_t(\varepsilon_{tx} - \varepsilon_{t0})/(\varepsilon_{tu} - \varepsilon_{t0})$$

$$\sigma_s = f_y + E_2(\varepsilon_s - s_{sy})$$

$$\sigma_s = E_s\varepsilon_s$$

Ultimate point

Cracking point

(a) concrete   (b) steel reinforcement   (c) BFRP grid   (d) ECC
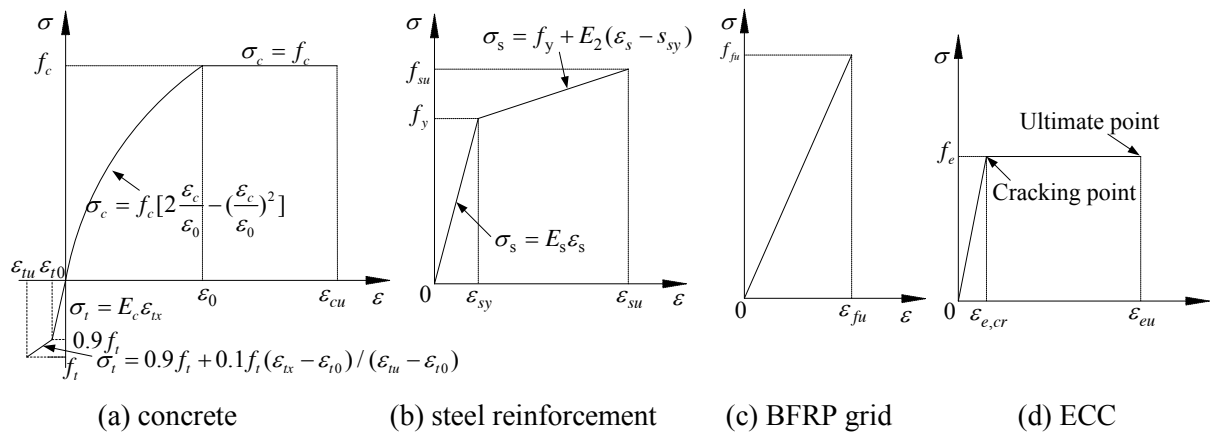
Fig.10 Stress-strain relationship models of all materials

Fig.11 Stress and strain distribution at different states, showing: (a) Cracking state; (b) Yielding state;

(c) Ultimate state

Fig.12 Relationship of mean sectional curvature and external moment

Table 1 Mixture proportion of ECC

Quantity (kg/m^3)						
Water	Cement	Flay ash	Quartz sand	Silica fume	Water reducer	PVA Fiber
1.4	1	4	0.15	0.15	0.05	0.06

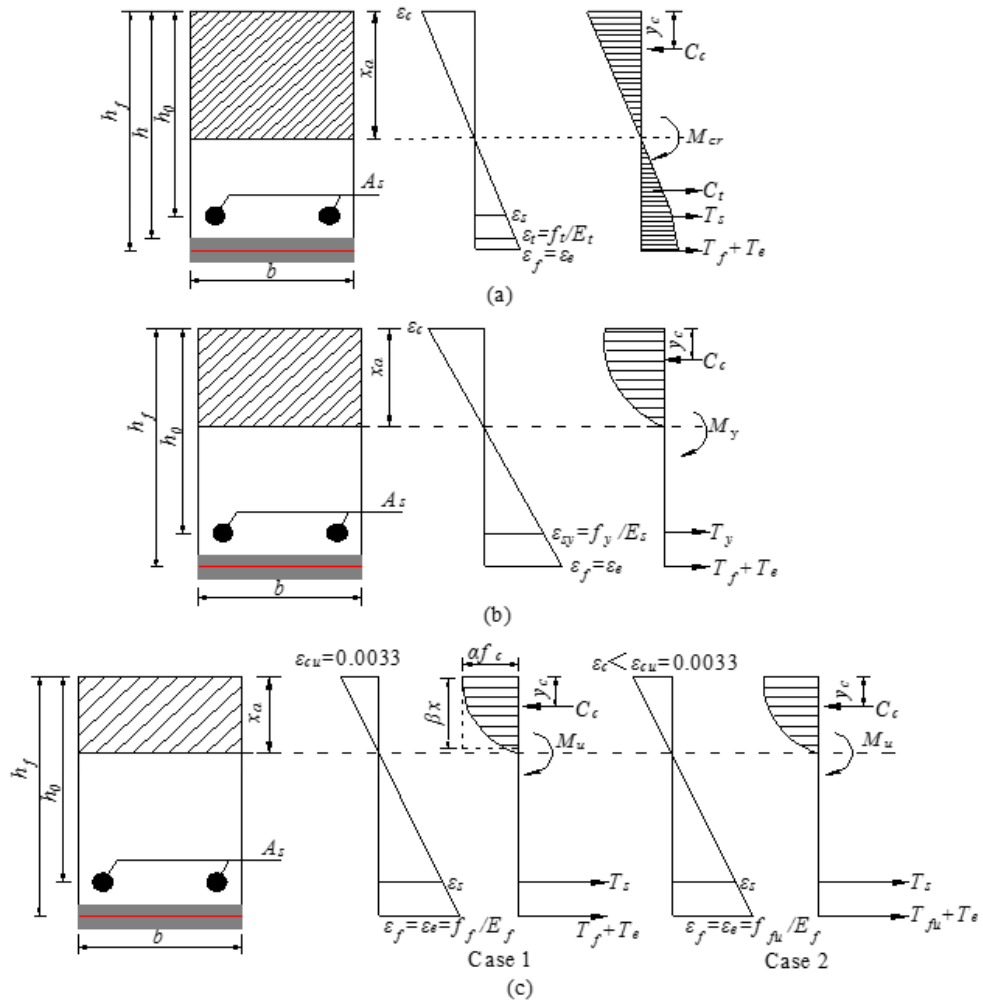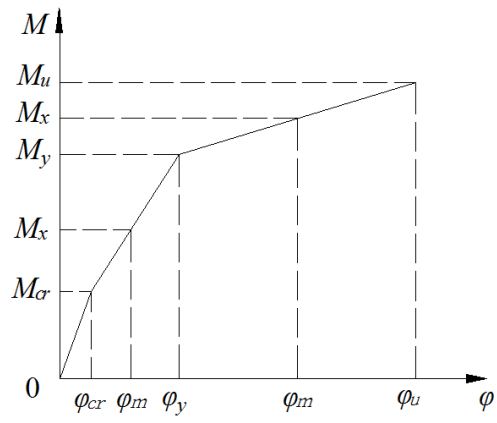Table 2 Details of test beams

Specimen	Concrete		ECC		Steel reinforcement		Thickness of BFRP grid/mm	Bond length of CRL l_f/mm	Distance from the support to CRL end a/mm
	f_{cu}(MPa)	E_c(GPa)	f_{ecc}(MPa)	E_{ecc}(GPa)	f_y(MPa)	E_s(GPa)			
CL							-	-	-
BB-1-500							1mm	500	100
BB-3-500	35.0	31.0	2.75	12.0	560	200	3mm	500	100
BB-5-500							5mm	500	100
BB-3-450							3mm	450	150
BB-3-400							3mm	400	200

Table 3 Summary of experimental and predicted results of all test beams: loads

Beam ID	Crack state			Yielding state			Ultimate state			Failure mode	
	$P_{cr,e}$ (kN)	$P_{cr,p}$ (kN)	$P_{cr,p}/P_{cr,e}$	$P_{y,e}$ (kN)	$P_{y,p}$ (kN)	$P_{y,p}/P_{y,e}$	$P_{u,e}$ (kN)	$P_{u,p}$ (kN)	$P_{u,p}/P_{u,e}$	Tested	Predicted
CL	31	38	1.23	101	110	1.09	126	120	0.96	C	C
BB-1-500	54	52	0.96	121	127	1.05	131	129	0.99	R+C	R
BB-3-500	61	52	0.85	126	130	1.03	146	139	0.96	R+C	R
BB-5-500	56	52	0.93	136	138	1.02	167	151	0.90	R+PD	R
BB-3-450	54	51	0.95	126	129	1.02	141	138	0.98	R+C	R
BB-3-400	49	50	1.02	116	128	1.11	136	136	1.00	R+C	R
Average			0.99			1.05			0.96		
SD			0.13			0.04			0.03		
COV			0.13			0.03			0.04		

Note: SD-standard deviation; COV-coefficient of variation; C-concrete crushing; R-rupture of BFRP grid; PD-partial debonding of composite strengthening layer.

Table 4 Summary of experimental and predicted results of all test beams: mid-span displacements

Beam ID	Crack state			Yielding state			Ultimate state		
	$D_{cr,e}$ (mm)	$D_{cr,p}$ (mm)	$D_{cr,p}/D_{cr,e}$	$D_{y,e}$ (mm)	$D_{y,p}$ (mm)	$D_{y,p}/D_{y,e}$	$D_{u,e}$ (mm)	$D_{u,p}$ (mm)	$D_{u,p}/D_{u,e}$
CL	0.25	0.31	1.24	4.42	4.53	1.02	25.88	31.03	1.20
BB-1-500	0.57	0.42	0.74	4.76	4.45	0.93	10.32	7.95	0.77
BB-3-500	0.60	0.42	0.70	4.38	4.37	1.00	10.51	8.39	0.80
BB-5-500	0.63	0.43	0.68	5.13	4.60	0.90	10.54	8.46	0.80
BB-3-450	0.49	0.40	0.82	4.56	4.40	0.96	9.80	8.37	0.85
BB-3-400	0.45	0.39	0.86	4.17	4.42	1.06	11.00	8.36	0.76
Average			0.84			0.98			0.86
SD			0.21			0.06			0.17
COV			0.25			0.06			0.19

Note: SD-standard deviation; COV-coefficient of variation.